Journal of
Materials Chemistry C

ROYAL SOCIETY
OF CHEMISTRY

PAPER

View Article Online
View Journal | View Issue

Check for updates

Cite this: *J. Mater. Chem. C*, 2023, **11**, 13725

Achieving dynamic quintuple-mode luminescence in $Ca_3Ti_2O_7$:Pr^{3+},Er^{3+} phosphor for anti-counterfeiting applications†

Jian Zhang,‡[a] Xin You,‡[a] Ting Wang, *[b] Yiyu Cai,[a] Chao Wang,[a] Xin Li,[a] Zhichao Liu,[a] Heng Dai,[a] Alexey Nikolaevich Yakovlev,[c] Xuhui Xu [a] and Jie Yu *[a]

Received 4th August 2023,
Accepted 14th September 2023

DOI: 10.1039/d3tc02783j

rsc.li/materials-c

Multi-mode luminescent materials refer to materials that can emit light at different wavelengths or colors depending on the applied stimulus, which could provide enhanced security features and make it more difficult for counterfeiters to reproduce. Here, we report the achievement of multi-color dynamic anti-counterfeiting by using multi-mode luminescence material $Ca_3Ti_2O_7$:Pr^{3+},Er^{3+} as the luminescent inks. $Ca_3Ti_2O_7$:Pr^{3+},Er^{3+} exhibits quintuple modes of photoluminescence (PL), long persistent luminescence (LPL), photo-stimulated luminescence (PSL), mechano-luminescence (ML), and up-conversion luminescence (UCL) with rich emission colors. The PL color of the phosphors could be modulated from red to yellow-green when the pump wavelength changes from 254 to 365 nm. Moreover, the tunable color of the phosphors is modulated from yellow to green by prolonging the irradiation time of a 980 nm laser (0.6 W), which is attributed to the elaborate cooperation of the PSL and UCL behaviors. Finally, the anti-counterfeiting trademark based on $Ca_3Ti_2O_7$:Pr^{3+}, $Ca_3Ti_2O_7$:Er^{3+} and $Ca_3Ti_2O_7$:Pr^{3+},Er^{3+} with attractive performance is designed for advanced anti-counterfeiting technology with exceptional security.

1. Introduction

Anti-counterfeiting technology refers to the practice of preventing the production and distribution of counterfeit, fake, or imitation products or items.[1–4] Luminescent materials have been widely utilized in stress sensing,[5] WLEDs,[6] anti-counterfeiting technology, and so on,[7,8] thanks to their advantages of low cost, high stability, facile design, and excellent concealment,[9–12] especially in the anti-counterfeiting technology field. Major breakthroughs have been made in recent years; however, most traditional luminescent anti-counterfeiting materials mainly depend on the single photoluminescence mode.[13] The single color always leads to easy decipherability because it is visible in the environment or only under UV light, which poses a security risk for manufacturers.[14–17] Therefore, developing effective, cost-effective, and non-forgeable anti-counterfeiting technology is a crucial goal to protect the rights and interests of consumers and legitimate businesses.[18–23]

Multi-modal luminescence anti-counterfeiting has drawn considerable attention under different types of stimuli, including excitation light, heat, mechanical force, *etc.*, further improving their security level.[24] For instance, Xu *et al.* designed $BaGd_2O_4$:Bi^{3+},Er^{3+} phosphor, which could emit blue, green, and orange light under the excitation of UV light at 980 nm and 1550 nm.[25] Guo *et al.* also proposed Ba_2GdTaO_6:Mn^{4+},Er^{3+} with three-mode luminescence by adjusting the excitation wavelength.[26] Xu *et al.* designed SrZnOS:Yb^{3+},Er^{3+}, with four-mode luminescence that responded to UV light, a 980 nm laser, loaded force, and X-rays.[27] However, these anti-counterfeiting features have static luminescence patterns and do not offer a high level of security since the authentication features can be easily identified and copied. Therefore, to elevate the information-security level, it is crucial to develop dynamic multicolor luminescence responses that are triggered by specific stimuli and exhibit unique patterns over time.[28,29] The typical dynamic luminescence of the phosphors involves LPL and PSL behaviors, which are related to the filling and release processes of carriers from the traps under distinct stimulations. For instance, Xia *et al.* proposed the $NaGdTi_2O_6$:Pr^{3+},Er^{3+} phosphor with multi-mode luminescence,

---

[a] Faculty of Materials Science and Engineering, Kunming University of Science and Technology, Kunming 650093, China. E-mail: yujie@kust.edu.cn

[b] College of Materials and Chemistry & Chemical Engineering, Chengdu University of Technology, Chengdu 610059, China. E-mail: wangtkm@foxmail.com

[c] T.F. Gorbachev Kuzbass State Technical University, Kemerovo 650000, Russia

† Electronic supplementary information (ESI) available. See DOI: https://doi.org/10.1039/d3tc02783j

‡ These authors contributed equally.

which could emit red LPL due to the release of carriers caused by thermal disturbance,[30] and Zhu *et al.* designed a multi-mode luminescence $Ba_2Zr_2Si_3O_{12}$:Eu^{2+},Er^{3+}, which possesses the blue-green PSL performance due to the release of carriers that responded to the 980 nm laser.[31] The materials reported before exhibit unicolor due to the release of carriers over time, which poses a huge risk of cracking. Therefore, developing temporal and spatial anti-counterfeiting materials with multi-color and multi-mode luminescence is a crucial method to improve the anti-counterfeiting level. Despite the significant improvement in anti-counterfeiting capabilities achieved by developing dynamic anti-counterfeiting materials, it is still necessary to have practical and feasible methods of visualizing the multi-mode behaviors for reading out information.[32]

Herein, we fabricated Pr^{3+}, Er^{3+} co-doped $Ca_3Ti_2O_7$ phosphors that exhibit dynamic multi-mode luminescence, including PL, LPL, PSL, UCL, and ML phenomena, enabling multi-mode luminescence and tunable color under different stimuli sources.[33] Notably, the red PSL and green UCL cooperated skillfully to realize multi-color *via* adjusting the pump power and irradiation time of a 980 nm laser.[34] Finally, multi-mode dynamic luminescence based on composition, excitation wavelength, and irradiation time was used to design and produce advanced anticounterfeiting patterns with quintuple-mode luminescence.

2. Experimental sections

2.1. Sample synthesis

The original materials include TiO_2 (99%, Aladdin), $CaCO_3$ (99.99%, Aladdin), H_3BO_3 (99.5%, Aladdin), Pr_6O_{11} (99.99%, Aladdin), and Er_2O_3 (99.99%, Aladdin). All these materials were used without further purification. A series of $Ca_3Ti_2O_7$:$x$$Pr^{3+}$ (x = 0.1%, 0.2%, 0.25%, 0.5%, and 0.75%), $Ca_3Ti_2O_7$:0.25%Pr^{3+},$y$$Er^{3+}$ (y = 0.25%, 0.5%, 1%, 3%, 5%, and 7%), and $Ca_3Ti_2O_7$:1%Er^{3+} phosphors were synthesized by the high-temperature solid-state reaction method. Based on the stoichiometric ratio of the chemical formula, the original materials were weighted and transferred into the agate mortar and mixed uniformly with the alcohol for 20 min, then put into an aluminum crucible (5 mL) in a furnace (1350 °C, 6 h, air). After naturally cooling to room temperature (RT), the samples were milled into powders for further characterization.

2.2. Optical film fabrication

The ML composited films were fabricated by uniformly mixing the sifted powders (600 mesh size) with PDMS(A) and PDMS(B) at a weight ratio of 5 : 14 : 1(m_{phosphor} = 1 g; $m_{\text{PDMS(A)}}$ = 2.78 g; $m_{\text{PDMS(B)}}$ = 0.22 g), followed by transferring the mixture into a cylindrical mold. Finally, the ML films were successfully shaped in the drying oven at 340 K for 3 h.

2.3. Characterization

An X-ray diffractometer (D8 ADVANCE/Germany Bruker) with Cu Kα irradiation (λ = 1.5405 Å) was utilized to measure the X-ray diffraction (XRD) patterns, and the corresponding patterns (10°–80°) were collected by operating at 30 KV and 20 mA with a step of 0.04°. Scanning electron microscopy (SEM) (Tescan China, Ltd) was applied to investigate the morphology and elemental mapping. A Hitachi F-7000 fluorescence spectrophotometer was applied to record the PL, photoluminescence excitation (PLE), UCL, and LPL spectra. Moreover, the UCL and PSL spectra were recorded using a 980 nm laser. A digital phosphor photometer (Zhejiang University three colors Instrument. Co. Ltd) was applied to record the LPL decay curves. The FJ-427A TL meter was applied to record the thermoluminescence (TL) curves (293–678 K). The ML spectra were collected by an optical fiber (Ocean Optics USB2000 + XR1-ES) in cooperation with an MS-T3001 multifunctional material surface property tester. Digital pictures were taken by a digital camera (Nikon D7100 with AF-S Micro-NIKKOR 105 mm f/2.8G IF-ED).

3. Results and discussion

$Ca_3Ti_2O_7$ possesses a typical Ruddlesden–Popper structure with the orthorhombic space group $Ccm2_1$ (Fig. 1a).[35] The unit of $Ca_3Ti_2O_7$ consists of two types of polyhedrons, where Ti^{4+} ions are coordinated by six oxygen ions to form [TiO_6] octahedrons, and Ca^{2+} ions are coordinated by eight oxygen ions to form [CaO_8] dodecahedrons. The XRD patterns of the $Ca_3Ti_2O_7$:$x$$Pr^{3+}$($x$ = 0.1%, 0.2%, 0.25%, 0.5%, 0.75%, and 1%), $Ca_3Ti_2O_7$:1%Er^{3+}, and $Ca_3Ti_2O_7$:0.25%Pr^{3+},$y$$Er^{3+}$($y$ = 0.25%, 0.5%, 1%, 3%, 5%, and 7%) samples are given in Fig. 1b and Fig. S1 (ESI†). All diffraction peaks of these samples match well with the standard patterns card (PDF#14-0151), and no impurities are detected, indicating that Pr^{3+} and Er^{3+} ions are successfully incorporated into the $Ca_3Ti_2O_7$ matrix. According to Hume-Rothery rules, the Pr^{3+} (r = 1.266 Å, coordination number (CN) = 8) and Er^{3+} (r = 1.144 Å, CN = 8) ions preferentially occupy the Ca^{2+} (r = 1.26 Å, CN = 8) site. The Rietveld refinement patterns of representative $Ca_3Ti_2O_7$:0.25%Pr^{3+},1%Er^{3+} are further calculated, as given in Fig. 1c, and the refinement factors are calculated to be R_p = 6.11%, R_{wp} = 8.24%, and χ^2 = 2.657, implying that the as-prepared Pr^{3+}/Er^{3+} co-doped $Ca_3Ti_2O_7$ phosphors are a single phase without impurity. Moreover, the scanning electron microscopy (SEM) images and the corresponding element mapping images are shown in Fig. 1d, demonstrating that Pr^{3+} and Er^{3+} are uniformly distributed in the $Ca_3Ti_2O_7$:Pr^{3+},Er^{3+} particle. Further, the EDS spectrum (Fig. S2, ESI†) reveals that the Pr^{3+} and Er^{3+} ions are successfully introduced into the $Ca_3Ti_2O_7$ matrix.

The PLE and PL spectra of the $Ca_3Ti_2O_7$:0.25%Pr^{3+} and $Ca_3Ti_2O_7$:1%Er^{3+} samples are measured, as shown in Fig. 2a. The PLE spectrum of $Ca_3Ti_2O_7$:0.25%Pr^{3+} phosphor exhibits a broad band ranging from 200 to 425 nm, which is ascribed to the $^3H_4 \rightarrow {}^3P_0$ transitions of Pr^{3+} ions. Under 324 nm excitation, the PL spectrum of $Ca_3Ti_2O_7$:0.25%Pr^{3+} exhibits a red emission peaking at 614 nm, which is attributed to the $^1D_2 \rightarrow {}^3H_4$ transition of Pr^{3+} ions.[36] The emission spectra of $Ca_3Ti_2O_7$:Pr^{3+} samples with different Pr^{3+} doping concentrations have almost

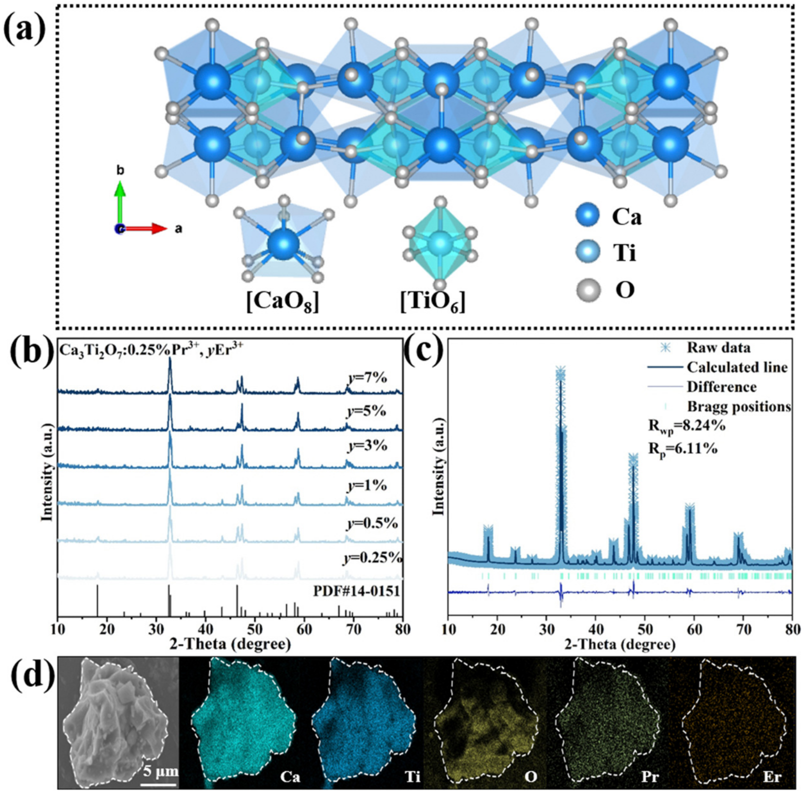

Fig. 1 (a) The crystal structure of $Ca_3Ti_2O_7$. (b) The XRD patterns of $Ca_3Ti_2O_7$:0.25%Pr^{3+},$y$$Er^{3+}$ (y = 0.25%, 0.5%, 1%, 3%, 5%, and 7%) phosphors. (c) The Rietveld refinement patterns of the representative $Ca_3Ti_2O_7$:0.25%Pr^{3+},1%Er^{3+} phosphor. (d) The SEM image and the corresponding elemental mapping images of the $Ca_3Ti_2O_7$:0.25%Pr^{3+},1%Er^{3+} crystal.

identical profiles, and the optimum doping concentration of Pr^{3+} is 0.25% (Fig. S3, ESI†). Additionally, the PLE spectrum of $Ca_3Ti_2O_7$:1%Er^{3+} shows a narrow band (350–410 nm), which can be assigned to $^4D_{15/2} \rightarrow {}^2G_{11/2}$ transitions of Er^{3+}. Under 380 nm excitation, the PL spectrum of $Ca_3Ti_2O_7$:1%Er^{3+} exhibits three emission peaks located at 525 nm, 552 nm, and 668 nm, which are, respectively, attributed to the $^2H_{11/2}$–$^4I_{15/2}$, $^4S_{3/2}$–$^4I_{15/2}$, and $^4F_{9/2} \rightarrow {}^4I_{15/2}$ transitions of Er^{3+}.[37,38]

Fig. 2b depicts the PL spectra of $Ca_3Ti_2O_7$:0.25%Pr^{3+},$y$$Er^{3+}$ (y = 0.25%, 0.5%, 1%, 3%, 5%, and 7%) under 365 nm excitation. With the increase in Er^{3+} ion content, the emission intensity at 614 nm gradually decreases, while the emission intensity of Er^{3+} increases and then decreases when the Er^{3+} concentration reaches 1% (Fig. 2c). The corresponding emission color is successfully modulated from red to yellow-green, as shown in Fig. 2d, and the corresponding CIE coordinates change from (0.6598, 0.3298) to (0.4690, 0.4533). Interestingly, the emission colors of $Ca_3Ti_2O_7$: 0.25%Pr^{3+},1%Er^{3+} are also flexibly modulated by changing the excitation wavelength due to the partially overlapped excitation of Pr^{3+} and Er^{3+} ions (Fig. 2e). The CIE coordinates of the representative $Ca_3Ti_2O_7$:0.25%Pr^{3+},1%Er^{3+} change from (0.5002, 0.3013) to (0.4917, 0.3157) when the excitation is modulated from 350 to 400 nm, which match well with the corresponding digital picture (Fig. 2f).

The LPL spectra of $Ca_3Ti_2O_7$:0.25%Pr^{3+},$y$$Er^{3+}$ (y = 0.25%, 0.5%, 1%, 3%, 5%, and 7%) samples exhibit obvious red LPL performance peaking at 614 nm, which is ascribed to the characteristic emission of Pr^{3+} ions, as given in Fig. 3a. The LPL intensity significantly enhances with the introduction of the Er^{3+} ions. Additionally, there is no emerging TL peak after the introduction of Er^{3+} ions, indicating that the introduction of Er^{3+} only increases the concentration of traps (Fig. S4 and S5, ESI†). Moreover, the LPL decay curves of $Ca_3Ti_2O_7$:0.25%Pr^{3+},$y$$Er^{3+}$ (y = 0.25%, 0.5%, 1%, 3%, 5%, and 7%) consisting of two parts at RT, a rapid decay process initially and a slow decay process, are displayed in Fig. 3b. The LPL performance is optimized when the concentration of Er^{3+} is 1%. Additionally, the corresponding TL curves of these samples are systematically measured, as shown in Fig. 3c. There is only one symmetric TL peak located at 324 K, which could be categorized as shallow traps. Moreover, $Ca_3Ti_2O_7$:0.25%Pr^{3+},1%Er^{3+} exhibits the highest TL intensity, which is well matched with the LPL intensity.

The emission spectra of $Ca_3Ti_2O_7$:0.25%Pr^{3+},1%Er^{3+} phosphors charged with 365 nm UV light for 5 min by continuously prolonging the 980 nm laser (0.6 W) irradiation time are investigated, as shown in Fig. 4a. The emission spectra exhibit three peaks at 525, 552, and 614 nm, where the emissions at 525 and 552 nm are ascribed to the UCL of Er^{3+} and the red emission at 614 nm is attributed to the PSL of Pr^{3+}. Herein, the emission intensity at 525 and 552 nm remains stable (Fig. S6, ESI†), while the emission intensity at 614 nm gradually drops and then vanishes when the 980 nm laser irradiation time

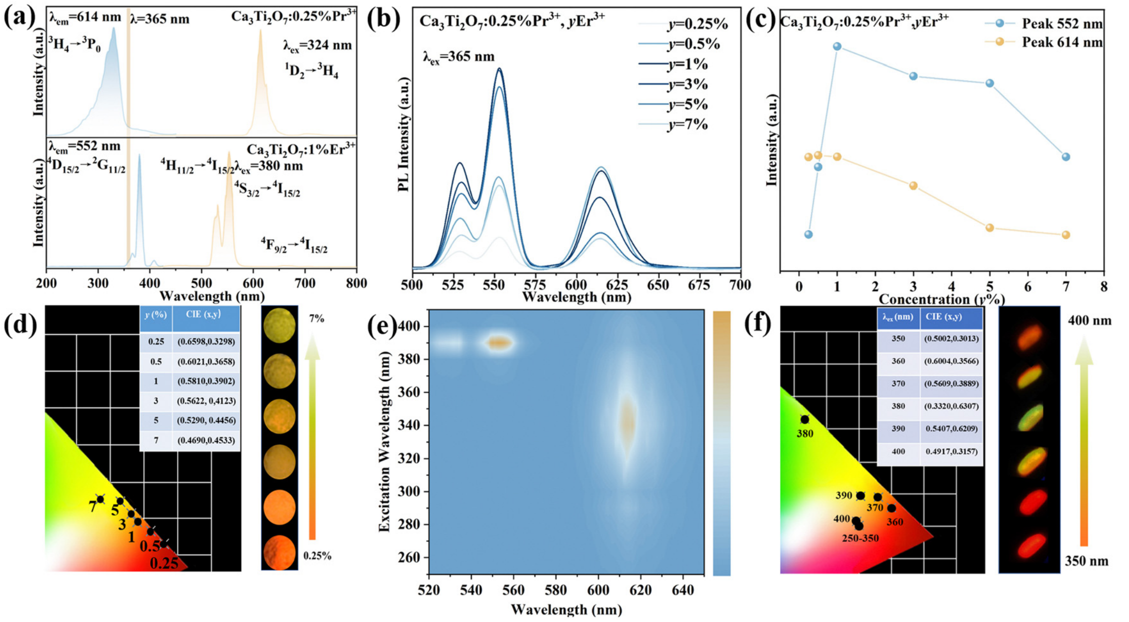

y (%)	CIE (x,y)
0.25	(0.6598,0.3298)
0.5	(0.6021,0.3658)
1	(0.5810,0.3902)
3	(0.5622, 0,4123)
5	(0.5290, 0.4456)
7	(0.4690,0.4533)

λ_{ex} (nm)	CIE (x,y)
350	(0.5002,0.3013)
360	(0.6004,0.3566)
370	(0.5609,0.3889)
380	(0.3320,0.6307)
390	0.5407,0.6209)
400	0.4917,0.3157)

Fig. 2 (a) The PLE and PL spectra of $Ca_3Ti_2O_7$:0.25%Pr^{3+} and $Ca_3Ti_2O_7$:1%Er^{3+} phosphors. (b) The PL spectra, (c) the corresponding emission intensity at 614 nm and 552 nm, and (d) the corresponding CIE coordinates and photographs of $Ca_3Ti_2O_7$:0.25%Pr^{3+},$y$$Er^{3+}$($y$ = 0.25%, 0.5%, 1%, 3%, 5%, and 7%) under 365 nm excitation. (e) Dependence of PL spectra and (f) the corresponding CIE coordinates and photographs of the representative $Ca_3Ti_2O_7$:0.25%Pr^{3+},1%Er^{3+} samples as a function of excitation wavelengths.

exceeds 21 s. The color of $Ca_3Ti_2O_7$:0.25%Pr^{3+},1%Er^{3+} tunes from yellow to green with increasing irradiation time, and the corresponding CIE ordinates change from (0.5818, 0.3951) to (0.3822, 0.6069), which is attributed to the cooperation of stable UCL and the decreasing PSL phenomenon. The TL curves of different pump powers of the 980 nm laser strongly prove that the low pump power (0.6 W) of the 980 nm laser caused the slow release of carriers from the traps and then resulted in a gradual decrease of the 614 nm emission. Moreover, the high pump power (1.5 W) of the 980 nm laser causes the instant release of carriers (Fig. S7, ESI†), which is consistent with the phenomenon. Fig. 4c plots the UCL intensity of $Ca_3Ti_2O_7$:0.25%Pr^{3+},1%Er^{3+} as a function of the 980 nm laser pump density, and the corresponding UCL emission intensities at 525 nm, 552 nm, and 668 nm gradually enhance with increasing pump power. Additionally, the relationship between emission intensity and pump density is studied based on the following equation:[39]

$$I \propto P^n \tag{1}$$

where I refers to the UCL intensity, P is the laser power, and n is the number of photons. The fitted linear slopes of 525 nm, 552 nm, and 668 nm are calculated to be 1.57, 1.56, and 1.51, respectively, indicating that the UCL process of $Ca_3Ti_2O_7$:0.25%Pr^{3+},1%Er^{3+} is a two-photon transition (Fig. 4d).

Fig. 5a illustrates the as-obtained $Ca_3Ti_2O_7$:0.25%Pr^{3+},1%Er^{3+}@PDMS composite film, which exhibits a smooth appearance and high flexibility (I and ii). The ML performance of the composite film was recorded using a digital camera with long-exposure technology, and the corresponding stress distribution could be extracted by using the gray value of the image (iii and v). Fig. S8 (ESI†) depicts a schematic diagram of the MS-T3001 multifunctional material surface property tester, which is used along with an optical fiber for mechano-luminescence spectrum analysis. Fig. 5b depicts the ML spectra of $Ca_3Ti_2O_7$:0.25%Pr^{3+},$y$$Er^{3+}$ (y = 0.25%,

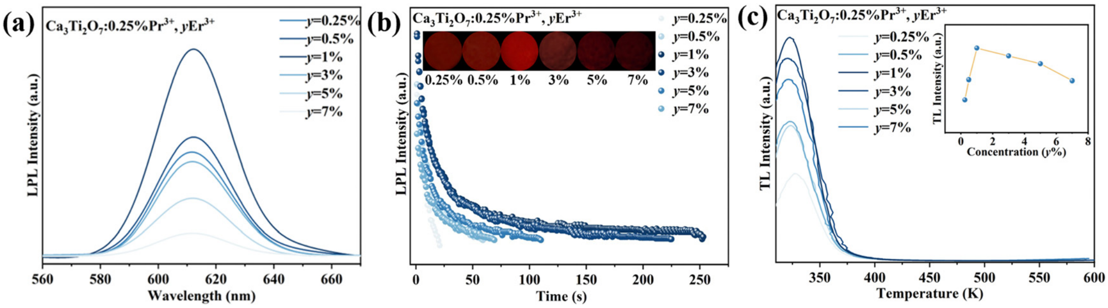

Fig. 3 (a) The LPL spectra, (b) the corresponding LPL decay curves, and (c) the TL curves of $Ca_3Ti_2O_7$:0.25%Pr^{3+},$y$$Er^{3+}$ (y = 0.25%, 0.5%, 1%, 3%, 5%, and 7%). The inset shows the digital pictures, and the samples were irradiated by a 365 nm UV lamp for 5 min.

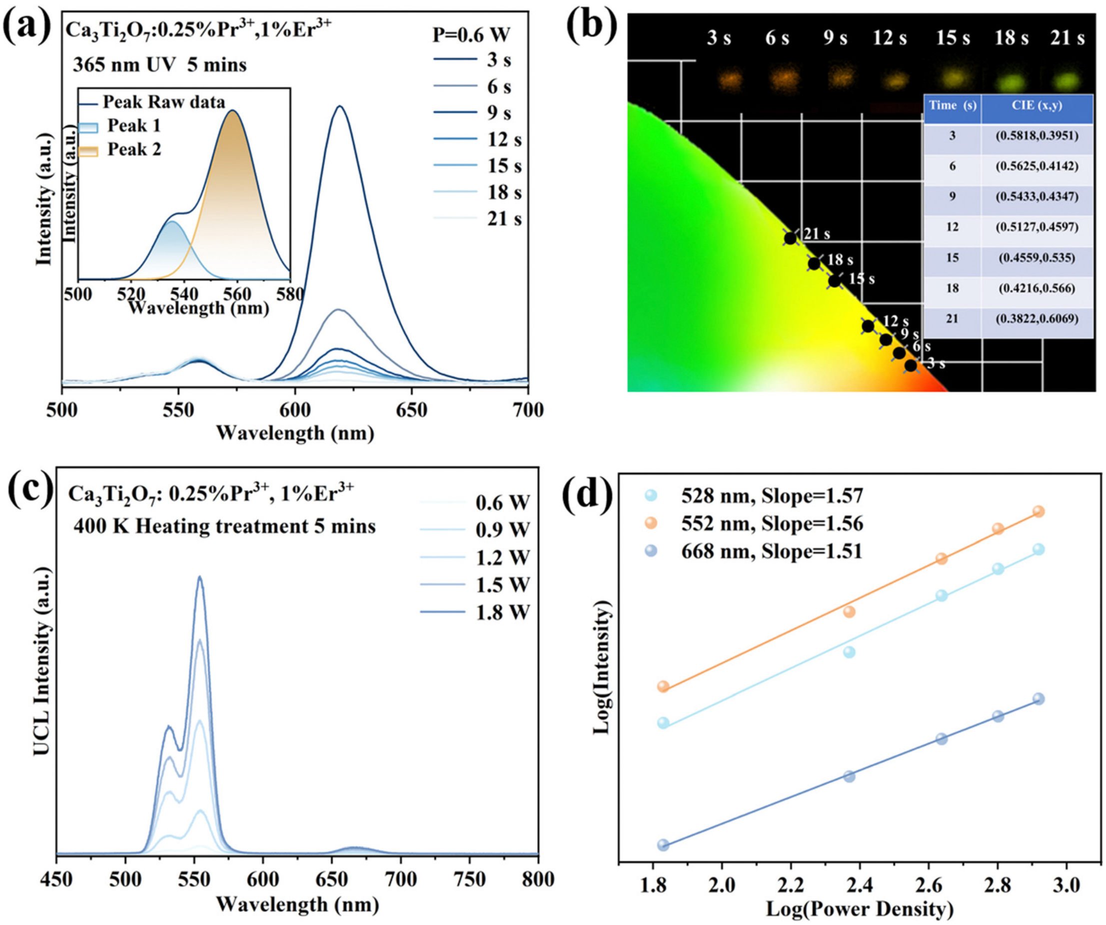

Time (s)	CIE (x,y)
3	(0.5818,0.3951)
6	(0.5625,0.4142)
9	(0.5433,0.4347)
12	(0.5127,0.4597)
15	(0.4559,0.535)
18	(0.4216,0.566)
21	(0.3822,0.6069)

Fig. 4 (a) The PSL–UCL spectra and (b) the corresponding CIE coordinates and photographs of $Ca_3Ti_2O_7$:0.25%Pr^{3+},1%Er^{3+} with prolonged 980 nm laser irradiation time; the pump density is 0.6 W (the samples were pre-irradiated with 365 nm UV light for 5 min). (c) The UCL spectra and (d) the corresponding emission of $Ca_3Ti_2O_7$:0.25%Pr^{3+},1%Er^{3+} as a function of pump density.

0.5%, 1%, 3%, 5%, and 7%), and the inset shows that the $Ca_3Ti_2O_7$:0.25%Pr^{3+},1%Er^{3+}@PDMS composite film exhibits the highest ML intensity. Moreover, the ML spectra exhibit the same profile and peak location as the PL spectrum of $Ca_3Ti_2O_7$:0.25%Pr^{3+}, confirming that the ML originates from the $^1D_2$–$^3H_4$ transition of Pr^{3+} ions. To investigate the ML mechanism of $Ca_3Ti_2O_7$:0.25%Pr^{3+},1%Er^{3+}@PDMS, the ML spectra of $Ca_3Ti_2O_7$:0.25%Pr^{3+},1%Er^{3+}@PDMS were measured after being charged with UV irradiation for 5 min and heating treatment at 400 K for 5 min (Fig. 5c). They show that $Ca_3Ti_2O_7$:0.25%Pr^{3+},1%Er^{3+}@PDMS after being charged with UV light exhibits strong red ML, while $Ca_3Ti_2O_7$:0.25%Pr^{3+},1%Er^{3+}@PDMS after being heated at 400 K displays no ML phenomenon. This preliminary evidence supports the fact that the ML phenomenon is attributed to the release of the carriers from the traps, as evident from the TL curves (Fig. S9, ESI†). Additionally, the TL curves of $Ca_3Ti_2O_7$:0.25%Pr^{3+},1%Er^{3+}@PDMS with prolonged stress duration are presented in Fig. 5d, which show a decreasing trend with increasing stress duration. This strongly supports the fact that the force could trigger the release of carriers from the traps. The aforementioned results indicate the ML performance of the as-obtained $Ca_3Ti_2O_7$:Pr^{3+},Er^{3+} material is determined by the traps. Fig. 5e displays the ML spectra of $Ca_3Ti_2O_7$:0.25%Pr^{3+},1%Er^{3+}@PDMS as a function of loaded stress. The ML intensity increases linearly with the increase in force, revealing that the as-fabricated composite film could be employed for quantitatively describing the applied force. In addition, the cycling stability of the ML film is systematically investigated, and the ML intensities of $Ca_3Ti_2O_7$:0.25%Pr^{3+},1%Er^{3+}@PDMS after experiencing continuous stress cycles and then being charged with UV light for 5 min are recorded in Fig. 5f. The ML peak intensity experiences a significant decay with the friction cycles. Moreover, $Ca_3Ti_2O_7$:0.25%Pr^{3+},1%Er^{3+}@PDMS possesses excellent reusability properties; after five reusability cycles, the initial ML intensity slightly decreases.

Inspired by the fascinating optical properties of $Ca_3Ti_2O_7$:Pr^{3+},Er^{3+}, cooperating with the properties of $Ca_3Ti_2O_7$:0.25%Pr^{3+} and $Ca_3Ti_2O_7$:1%Er^{3+} (Fig. S10, ESI†), a trademark concept is designed consisting of $Ca_3Ti_2O_7$:0.25%Pr^{3+},1%Er^{3+}, $Ca_3Ti_2O_7$:0.25%Pr^{3+} and $Ca_3Ti_2O_7$:1%Er^{3+} *via* screen printing technology (Fig. 6a). Fig. 6b reveals the individual components of each section of the trademark. The "Cat", "Dog", and "Horse" portions are printed with $Ca_3Ti_2O_7$:0.25%Pr^{3+},1%Er^{3+}@PDMS, $Ca_3Ti_2O_7$:0.25%Pr^{3+}@PDMS, and $Ca_3Ti_2O_7$:1%Er^{3+}@PDMS ink, respectively. Under 254 nm UV light, the trademark displays a

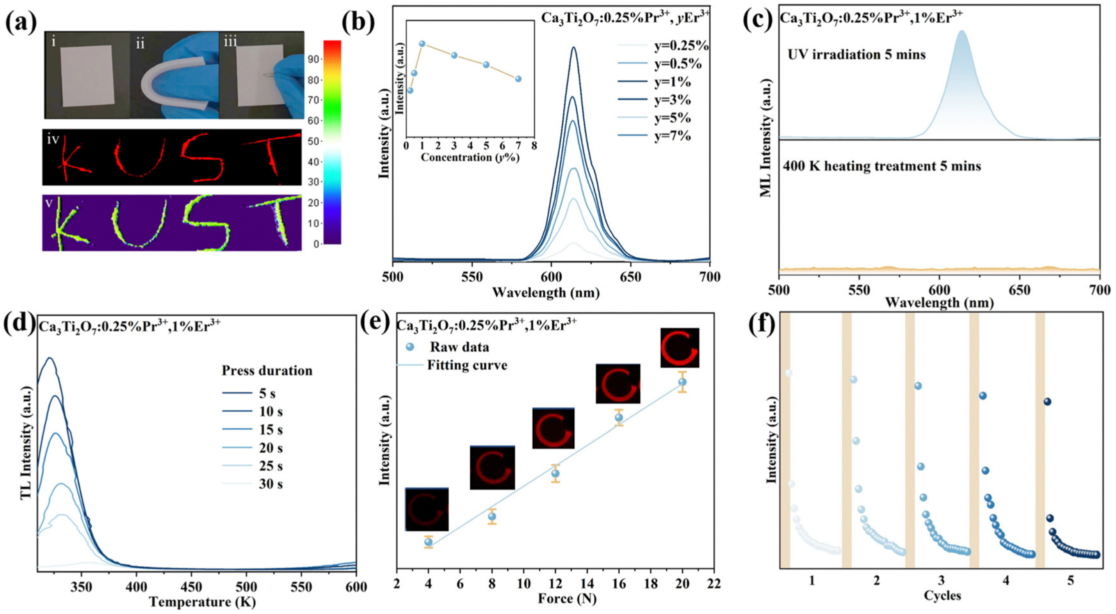

Fig. 5 (a) The appearance and flexibility of the $Ca_3Ti_2O_7$:0.25%Pr^{3+},1%Er^{3+}@PDMS ML composite film, and the corresponding photographs and dimensional color map under mechanical stimulation. (b) The ML intensity of $Ca_3Ti_2O_7$:0.25%Pr^{3+},$y$$Er^{3+}$@PDMS ($y$ = 0.25%, 0.5%, 1%, 3%, 5%, and 7%) under 10 N force. (c) The ML spectra of $Ca_3Ti_2O_7$:0.25%Pr^{3+},1%Er^{3+}@PDMS film after being charged with UV irradiation for 5 min and heating treatment at 400 K for 5 min, respectively. (d) The TL curves of $Ca_3Ti_2O_7$:0.25%Pr^{3+},1%Er^{3+}@PDMS as a function of the press duration. (e) The ML intensity of $Ca_3Ti_2O_7$:0.25%Pr^{3+},1%Er^{3+}@PDMS as a function of the stretching stress; the insets show the corresponding photographs. (f) The ML recovery behavior and reproducibility of $Ca_3Ti_2O_7$:0.25%Pr^{3+},1%Er^{3+}@PDMS after being charged with UV irradiation for 5 min.

red "Dog" pattern, while under 365 nm UV light, the trademark exhibits yellow "Cat", red "Dog", and green "Horse" patterns. Interestingly, after being exposed to 365 nm UV light for 5 min, the trademark features the brighter red "Dog" pattern and the darker red "Cat" pattern. There is only a darker red "Cat" pattern when the UV light is ceased for 100 s, and all patterns vanish at 250 s. Additionally, the trademark gradually changes from the yellow "Cat", red "Dog", and green "Horse" patterns to green "Cat" and green "Horse" patters when continually irradiated by a 980 nm laser (0.6 W) for 20 s. When the pump

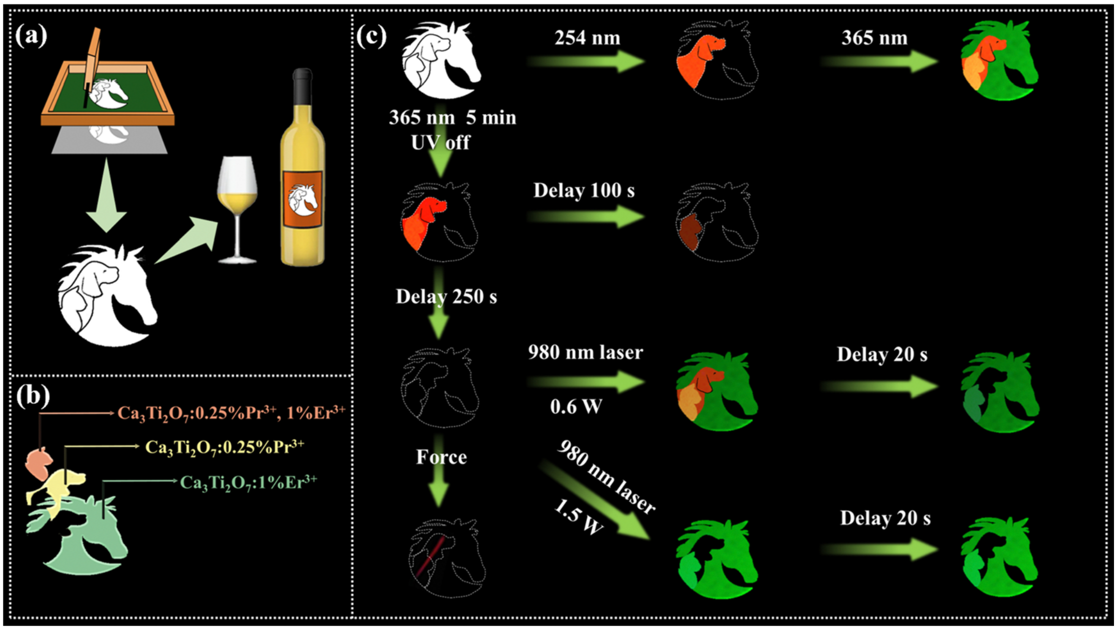

Fig. 6 (a) The fabrication process and application of the trademark. (b) The specific components of each part of the trademark. (c) The PL, LPL, ML, and PSL–UCL photographs of the phosphor stimulated by 254 nm light, 365 nm light, thermal disturbance, a 980 nm laser (0.6 W, 1.5 W), and force, respectively.

density is increased to 1.5 W, the trademark exhibits stable green ''Cat'' and green ''Horse'' patterns by continually prolonging the irradiation time. Under the stimulation of stress, a bright red ML is observed by rubbing the trademark with a glass rod. Based on the PL, LPL, PSL, UCL, and ML properties, the trademark can achieve dynamic anti-counterfeiting with heterogeneous readout methods. This is a significant advantage for the applications of information encryption and anti-counterfeiting.

4. Conclusion

In summary, we have successfully synthesized $Ca_3Ti_2O_7:Pr^{3+},Er^{3+}$ phosphor with multi-mode luminescence, which includes PL, LPL, PSL, UCL, and ML properties. $Ca_3Ti_2O_7:Pr^{3+},Er^{3+}$ emits red and yellow light under 254 nm or 365 nm light, respectively, and exhibits red LPL, ML, and PSL, and green UCL behaviors. Notably, the emission colors of $Ca_3Ti_2O_7:Pr^{3+},Er^{3+}$ can be modulated from yellow to green upon continuous irradiation by a 980 nm laser with a low pump power of 0.6 W. However, when the pump power increases to 1.5 W, the output colors remain green over time. Finally, the multi-mode luminescence of $Ca_3Ti_2O_7:Pr^{3+},Er^{3+}$, which cooperated with $Ca_3Ti_2O_7:Pr^{3+}$ and $Ca_3Ti_2O_7:Er^{3+}$, has enabled the realization of dynamic anti-counterfeiting. Our work introduces a novel approach for designing multi-mode anti-counterfeiting technology with a high level of security.

Author contributions

Jian Zhang: conceptualization, methodology, validation, methodology. Xin You: writing, resources. Ting Wang: writing—review and editing. Yiyu Cai: project administration. Chao Wang: data curation. Xin Li: software, investigation. Zhichao Liu: writing—review and editing. Heng Dai: resources. Alexey Nikolaevich Yakovlev: resources. Xuhui Xu: supervision. Jie Yu: funding acquisition, supervision, writing—review and editing.

Conflicts of interest

The authors declare that they have no known competing financial interests or personal relationships that could have appeared to influence the work reported in this paper.

Acknowledgements

This work was financially supported by the National Nature Science Foundation of China (NSFC) (61965012), the Science and Technology Major Project of Yunnan Province (202002AB080001), Deep UV Stimulated Emission Performance Based on Glass Ceramics as an Optical Gain Medium (KKYB201951001, 2019FI001), and the International Joint Innovation Platform of Yunnan Province (202203AP140004).

References

1 K. Du, J. Feng, X. Gao and H. Zhang, *Light: Sci. Appl.*, 2022, **11**, 222.
2 X. Feng, Y. Sheng, K. Ma, F. Xing, C. Liu, X. Yang, H. Qian, S. Zhang, Y. Di, Y. Liu and Z. Gan, *Adv. Opt. Mater.*, 2022, **10**, 2200706.
3 D. Gao, Q. Kuang, F. Gao, H. Xin, S. Yun and Y. Wang, *Mater. Today Phys.*, 2022, **27**, 100765.
4 X. Han, E. Song, B. Zhou and Q. Zhang, *J. Mater. Chem. C*, 2019, **7**, 8226–8235.
5 T. Zheng, M. Runowski, J. Xue, L. Luo, U. R. Rodríguez-Mendoza, V. Lavín, I. R. Martín, P. Rodríguez-Hernández, A. Muñoz and P. Du, *Adv. Funct. Mater.*, 2023, **33**, 2214663.
6 P. Du, J. Tang, W. Li and L. Luo, *Chem. Eng. J.*, 2021, **406**, 127165.
7 J. Liu, Y. Liang, S. Yan, D. Chen, S. Miao, W. Wang and J. Bi, *J. Mater. Chem. C*, 2021, **9**, 9692–9701.
8 S. Yan, Y. Liang, J. Liu, D. Chen, S. Miao, J. Bi and K. Sun, *J. Mater. Chem. C*, 2021, **9**, 14730–14739.
9 K. Huang, X. Dou, Y. Zhang, X. Gao, J. Lin, J. Qu, Y. Li, P. Huang and G. Han, *Adv. Funct. Mater.*, 2021, **31**, 2009920.
10 K. Jiang, L. Zhang, J. Lu, C. Xu, C. Cai and H. Lin, *Angew. Chem., Int. Ed.*, 2016, **55**, 7231–7235.
11 T. Jiang, Y. F. Zhu, J. C. Zhang, J. Zhu, M. Zhang and J. Qiu, *Adv. Funct. Mater.*, 2019, **29**, 1906068.
12 Y. Li, M. Gecevicius and J. Qiu, *Chem. Soc. Rev.*, 2016, **45**, 2090–2136.
13 L. Liang, J. Chen, K. Shao, X. Qin, Z. Pan and X. Liu, *Nat. Mater.*, 2023, **22**, 289–304.
14 Z. Liu, L. Zhao, W. Chen, X. Fan, X. Yang, S. Tian, X. Yu, J. Qiu and X. Xu, *J. Mater. Chem. C*, 2018, **6**, 11137–11143.
15 P. Pei, Y. Bai, J. Su, Y. Yang and W. Liu, *Sci. China Mater.*, 2022, **65**, 2809–2817.
16 P. Pei, K. Liu, Z. Ju, R. Wei and W. Liu, *J. Mater. Chem. C*, 2022, **10**, 5240–5248.
17 H. Suo, Q. Zhu, X. Zhang, B. Chen, J. Chen and F. Wang, *Mater. Today Phys.*, 2021, **21**, 100520.
18 S. Vaidyanathan, *J. Mater. Chem. C*, 2023, **11**(26), 8649–8687.
19 J. Xu, B. Zhang, L. Jia, Y. Fan, R. Chen, T. Zhu and B. Liu, *ACS Appl. Mater. Interfaces*, 2019, **11**, 35294–35304.
20 Z. Xu, Y. Zhu, Q. Luo, X. Liu and L. Li, *J. Lumin.*, 2020, **219**, 116894.
21 Y. L. Yang, T. Li, F. Guo, J. Y. Yuan, C. H. Zhang, Y. Zhou, Q. L. Li, D. Y. Wan, J. T. Zhao and Z. J. Zhang, *Inorg. Chem.*, 2022, **61**, 4302–4311.
22 J. C. Zhang, C. Pan, Y. F. Zhu, L. Z. Zhao, H. W. He, X. Liu and J. Qiu, *Adv. Mater.*, 2018, **30**, e1804644.
23 R. N. E. Zhen Li, M. E. Light, E. Ruiz, F. Teixidor, C. Viñas, D. Ruiz-Molina,C. Roscini and J. Giner Planas, *Chem. Mater.*, 2022, **34**, 4795–4808.
24 J. G. Dangli Gao, F. Gao, Q. Kuang, Y. Pan, Y. Chenb and Z. Pan, *J. Mater. Chem. C*, 2021, **9**, 16634.
25 J. Fu, L. Zhou, Y. Chen, J. Lin, R. Ye, L. Lei, Y. Shen, D. Deng and S. Xu, *J. Am. Ceram. Soc.*, 2022, **106**, 1333–1343.
26 M. Jin, Y. Wu, Z. Zhang, J. Xiang and C. Guo, *Opt. Laser Technol.*, 2022, **152**, 108144.

27 Y. Zhao, G. Bai, Y. Huang, Y. Liu, D. Peng, L. Chen and S. Xu, *Nano Energy*, 2021, **87**, 106177.
28 H. Guo, T. Wang, X. Zhu, H. Liu, L. Nie, L. Guo, T. Gu, X. Xu and X. Yu, *J. Colloid Interface Sci.*, 2023, **640**, 719–726.
29 L. Guo, T. Wang, Q. Wang, W. Feng, Z. Li, S. Wang, P. Xia, F. Zhao and X. Yu, *Chem. Eng. J.*, 2022, **442**, 136236.
30 X. Zhou, L. Ning, J. Qiao, Y. Zhao, P. Xiong and Z. Xia, *Nat. Commun.*, 2022, **13**, 7589.
31 X. Zhu, T. Wang, Z. Liu, Y. Cai, C. Wang, H. Lv, Y. Liu, C. Wang, J. Qiu, X. Xu, H. Ma and X. Yu, *Inorg. Chem.*, 2022, **61**, 3223–3229.
32 B. Zhou, G. Xiao and D. Yan, *Adv. Mater.*, 2021, **33**, e2007571.
33 S. Tian, H. Zhang, X. Yang, L. Yang, Q. Min, H. Ma, X. Yu, J. Qiu and X. Xu, *Chem. Eng. J.*, 2021, **412**, 128695.
34 F. Liu, Y. Liang and Z. Pan, *Phys. Rev. Lett.*, 2014, **113**, 177401.
35 X.-H. Fan, J.-C. Zhang, M. Zhang, C. Pan, X. Yan, W.-P. Han, H.-D. Zhang, Y.-Z. Long and X. Wang, *Opt. Express*, 2017, **25**, 14238–14246.
36 B. Wang, H. Lin, J. Xu, H. Chen, Z. Lin, F. Huang and Y. Wang, *Inorg. Chem.*, 2015, **54**, 11299–11306.
37 Z. Wang, P. Pei, D. Bai, S. Zhao, X. Ma and W. Liu, *Inorg. Chem. Front.*, 2020, **7**, 2506–2514.
38 Y. Jia, Z. Shi, J. Wang, X. Li and Z. Zhao, *J. Lumin.*, 2023, **253**, 119489.
39 K. Wu, E. Wang, J. Yuan, J. Zuo, D. Zhou, H. Zhao, Y. Luo, L. Zhang, B. Li, J. Zhang, L. Tu and H. Zhang, *Angew. Chem., Int. Ed.*, 2023, e202306585, DOI: 10.1002/anie.202306585.